Article

Highly Resistant LaCo$_{1-x}$Fe$_x$O$_3$ Perovskites Used in Chlorobenzene Catalytic Combustion

Héctor Acosta Pérez [1], Carlos A. López [1], Octavio J. Furlong [2], Marcelo S. Nazzarro [2], Sergio G. Marchetti [3], Luis E. Cadús [1,*] and Fabiola N. Agüero [1]

[1] Instituto de Investigaciones en Tecnología Química (INTEQUI), Universidad Nacional de San Luis—Consejo Nacional de Investigaciones Científicas y Ténicas, Almirante Brown 1455, San Luis CP 5700, Argentina

[2] Instituto de Física Aplicada (INFAP), UNSL—CONICET, Av. Ejército de los Andes 950, San Luis CP 5700, Argentina

[3] Centro de Investigación y Desarrollo en Ciencias Aplicadas (CINDECA—CONICET), Universidad Nacional de La Plata, La Plata, Calle 47 N° 257, Buenos Aires CP 1900, Argentina

[*] Correspondence: lcadus@unsl.edu.ar

Abstract: The stability of LaCo$_{1-x}$Fe$_x$O$_3$ perovskite structures (x = 0; 0.25; 0.5; 0.75; 1) was studied in the combustion of chlorobenzene. This family of catalysts was synthesized by the citrate method obtaining pure structures. The Fe doping in the original structure induces electronic environments capable of generating the Co^{2+}/Co^{3+} redox couple. The characteristics observed in bulk are perfectly reflected on the surface, favoring a high resistance of the solids to chlorine poisoning. Superior stability under reaction conditions was observed in the phase with the lowest Fe content (x = 0.25), remaining stable at 100% combustion of chlorobenzene during 100 h, not observing intermediate reaction products. These results open up a new avenue for designing and fabricating high-performance catalysts in the environmental field

Keywords: perovskite; chlorobenzene; catalytic combustion; stability; cobalt; iron

1. Introduction

The removal of atmospheric pollutants is currently one of the pillars of international scientific research. The specific case of chlorinated volatile organic compounds (VOCs-Cl) has become very important in recent years due to their persistence and toxicity in the atmosphere [1]. The removal routes have been multiple, from the most conventional to the most promising [2,3]. One of the most effective ways to remove gaseous atmospheric pollutants in recent years has been by catalytic combustion, and within it, the use of inorganic structures of mixed oxides, specifically perovskites [4]. The combustion of chlorobenzene (CB) has been studied with similar structures, such as La$_{1-x}$Ca$_x$FeO$_3$, LaMnO$_3$, LaCoO$_3$, and YCoO$_3$ [5,6]. In a previous publication, the use of a LaCoO$_3$ structure substituted with Ce in the A position of the perovskite was studied in the combustion of chlorobenzene. These catalysts presented good stability that was correlated with the redox characteristics and great oxygen mobility due to the insertion of Ce into the structure, and it was found that there is a permissible limit of incorporation of Ce in the A position of the perovskite structure [7]. Mn and Fe cations have also been studied, giving promising results in this type of reaction [8,9]. The substitution of lanthanides in the A position (La, Ce) and the influence of different transition metals, such as Co, Mn, Fe, Ni, and many others, in the B position, have been studied. It can be inferred that the cations redox couple in a structure induces oxygen mobility that favors an exchange between the crystalline structure and the surface. These are the advantages desired from Fe in this type of reaction, as well as the easy insertion within the structure, providing pure phases in accordance with the orthorhombic geometry of the structures [10]. Additionally, due to the high availability and low price of iron precursors, the interest in ferrites has continued to grow over time, seeking strategies

to stabilize iron in oxidation states (III) and (IV) in these cubic systems, and considered as a prerequisite for the good catalytic activity of the material [11]. In addition, a structure combined with Fe in the perovskite B position could stabilize the system and provide greater stability in the reaction under study, as Fe can occupy active sites that originate electronic environments that lead to the generation of Co^{2+}, which is one of the main factors responsible for the good perovskite activity in this reaction [12]. In addition, Fe can also generate oxygen mobility from the lattice to the surface providing stability in the structure. In the search for catalysts with a high resistance to Cl poisoning in Cl-VOCs combustion, there has been much effort. However, there is still the need to design structures with high stability during long time periods. The aim of this work is to validate the hypotheses regarding the effect of the substitution of the B site by Fe in different proportions in $LaCoO_3$ perovskites, seeking improvements in the catalytic activity and stability of these substituted structures in the chlorobenzene combustion reaction.

2. Results and Discussion

2.1. Catalytic Activity

The prepared catalysts were studied in the combustion reaction of chlorobenzene (CB). The results of the catalytic activity are shown in Figure 1 and Table 1, the temperature values corresponding to the 50% conversion of CB (T_{50}), the 90% conversion of CB (T_{90}), and the balances of carbon and moles of Cl_2 produced after reaction are reported.
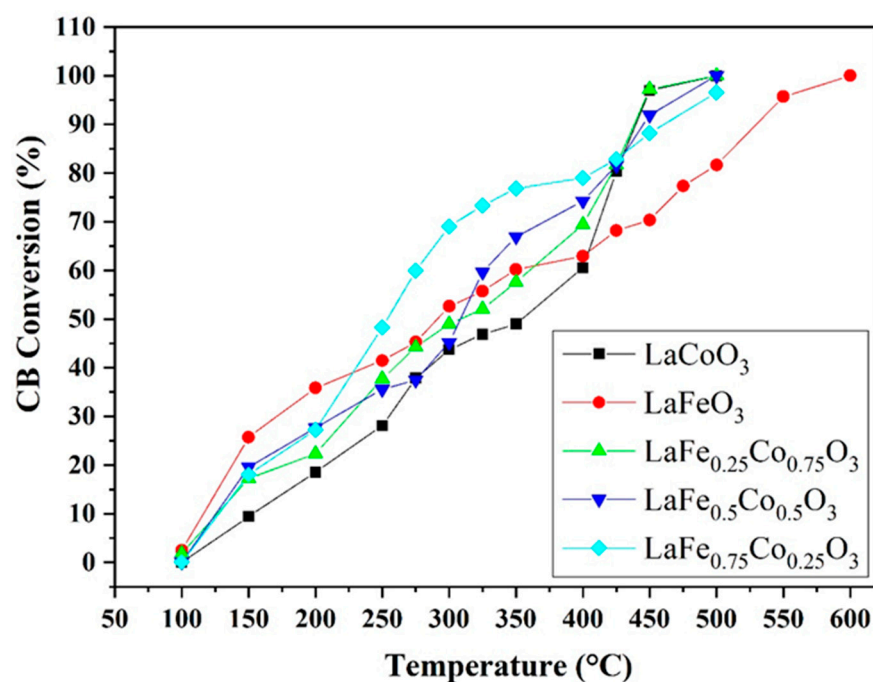

Figure 1. Catalytic activity results. Chlorobenzene conversion vs. reaction temperature.

Table 1. T_{50}, T_{90}, carbon, and Cl_2 balances for the synthesized catalysts.

Catalyst	T_{50}	T_{90}	Carbon Balance (%)	Cl_2 Moles of the Reaction Products
$LaCoO_3$	350.5	444.7	0.2	1.05×10^{-3}
$LaCo_{0.75}Fe_{0.25}O_3$	313.8	437.3	0.1	1.11×10^{-3}
$LaCo_{0.5}Fe_{0.5}O_3$	307.9	446.2	0.3	1.07×10^{-3}
$LaCo_{0.25}Fe_{0.75}O_3$	251.9	449.1	0.2	1.12×10^{-3}
$LaFeO_3$	288.7	528.6	0.3	1.14×10^{-3}

The small differences observed in the T90 values do not present a linear relationship with the increase or decrease in Fe content in the perovskite. However, T50 values decrease with the increase in Fe content. The catalyst that presented the lowest T_{50} was $LaCo_{0.25}Fe_{0.75}O_3$, whereas the lowest T_{90} was determined with $LaCo_{0.75}Fe_{0.25}O_3$. At low temperatures, the structures with the highest Fe content resulted in more activity, whereas at high temperatures (from 400 °C), the most active structures were those with the lowest content of this cation.

To corroborate that the catalysts completely convert the CB to its complete combustion products, the total carbon balances were carried out by the indirect method through the valuation of carbonates retained in a trap solution placed at the outlet of the reactor. The carbon balance closed between 0.1 and 0.3%, values that are considered within the error allowed in the calculation of this magnitude (Table 1). In the same way, the analysis of $Cl_2(g)$ was carried out as an oxidation product of this type of Cl-VOC. Considering that 1.18×10^{-3} moles of this compound should be obtained as a product under the reaction conditions, the number of moles of $Cl_2(g)$ obtained from this measurement correlated perfectly with the moles of this oxidation product considering a CB complete oxidation (Table 1).

Kamal et al. reported the CB combustion using mixed oxide-type catalysts (Co_3O_4/Alumina and SnO/MnO/TiO/CrO). They observed that the main cause of deactivation was the saturation of chlorine on the surface and the subsequent formation of intermediates such as organic acids and oxychlorides of the corresponding metals. As was explained in this work, these intermediaries could become more dangerous than the Cl-VOCs to be eliminated [13]. Rochard et al. detected the formation of intermediates such as benzyl alcohol and toluene during the CB combustion using spinel and perovskite-type catalysts ($Mn_{0.75}Co_{2.25}O_3$ and $La_{0.9}Sr_{0.1}CoO_3$). These intermediates caused the loss of the catalysts' activity and were the subject of further study due to their high persistence and toxicity compared to that of the VOCs under study [14]. In the present work, although some minimal differences can be distinguished in the balances of total carbon and Cl_2 that could be associated with the adsorption of Cl on the surface of the catalyst once the reaction has finished, the balances and the total conversion indicated that there was no formation of intermediates or oxychlorides at the end of the reaction test, unlike previously published works. It is worth mentioning that the formation of intermediates at low reaction temperatures cannot be discarded as in situ spectroscopy techniques should be necessary to corroborate it. In addition, the stability of the catalysts was studied under the same reaction conditions but at a fixed temperature, corresponding to the 100% conversion of CB. Figure 2 shows the variation of the chlorobenzene conversion as a function of time.

As can be seen, the catalyst that began to deactivate in the shortest time was $LaCoO_3$, showing a conversion below 50% after approximately 54 h, while the one that deactivated more quickly (around 45 h) was the catalyst that does not have cobalt in its structure, $LaFeO_3$. On the other hand, the most stable catalysts were those with the lowest Fe content (25% and 50%, respectively). The $LaCo_{0.5}Fe_{0.5}O_3$ catalyst began to deactivate after 50 h, reaching a value of 50% conversion at 65 h. On the other hand, the $LaCo_{0.75}Fe_{0.25}O_3$ catalyst presented excellent stability, maintaining the CB conversion at 100% during the 100 h of reaction without presenting deactivation over time.

A similar study carried out by Wang et al. showed CB conversion to 100% during 9–10 h using Fe-mixed oxide-type catalysts doped with Ni. In this case, despite the excellent results reported, they associated the low stability with the accumulation of Cl in the active sites [15]. Liu et al. reported a stability of 100% CB conversion for 20 h using perovskite-type catalysts ($SmMnO_3$) in different proportions of the cations. In this work, these authors informed that a higher proportion of acid sites improved the catalytic capacity, and they also observed that the deactivation of this type of catalyst occurred due to surface poisoning by residual Cl as a product of the combustion reaction [16]. Effectively, these recently published results evidence the excellent stability of the catalysts presented in our work. In general, the catalysts' stability increased in the following order: $LaFeO_3 < LaCoO_3 <$

$LaCo_{0.25}Fe_{0.75}O_3 < LaCo_{0.5}Fe_{0.5}O_3 < LaCo_{0.75}Fe_{0.25}O_3$. In order to find the reason for this catalyst stability order, an exhaustive characterization was created and discussed in the following sections.
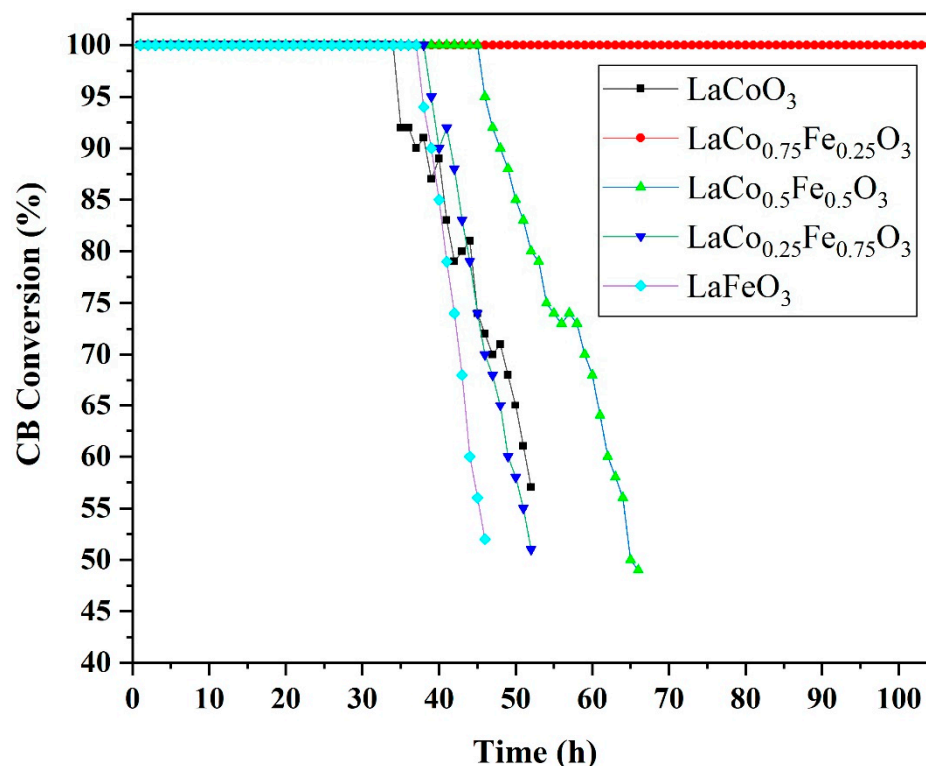

Figure 2. Stability test of chlorobenzene conversion as a function of reaction time.

2.2. Physicochemical Characterization of the Catalysts

The results of the S_{BET} analysis are presented in Table 2. The isotherms could be classified according to the IUPAC as type 3 at low pressures and type 5 at high pressures, being in all cases mesoporous materials, since all the isotherms presented H3-type hysteresis.

Table 2. Results of the BET isotherm analysis and H_2 consumption from the TPR study.

Catalysts	Surface Area (m²/g)		H₂ Consumption	Porous Volume (cm³/g)		Porous Diameter (Å)	
	Fresh	Used	(Moles H₂/g Co)	Fresh	Used	Fresh	Used
$LaCoO_3$	8.9	6.6	6.3×10^{-6}	0.058	0.031	261.12	188.62
$LaCo_{0.75}Fe_{0.25}O_3$	9.8	7.6	2.8×10^{-6}	0.073	0.041	295.95	213.89
$LaCo_{0.5}Fe_{0.5}O_3$	7.4	6.9	2.7×10^{-6}	0.037	0.030	200.02	174.91
$LaCo_{0.25}Fe_{0.75}O_3$	7.7	6.7	2.4×10^{-6}	0.061	0.024	317.24	144.57
$LaFeO_3$	6.5	6.1	–	0.052	0.074	319.87	486.78

The partial substitution of the B position by 25% of Fe slightly increased the original surface area of the $LaCoO_3$ catalyst. At higher substitution percentages, the surface areas decreased due to the change in geometry that occurs in the structure, although the variations do not reflect a linear relationship. The largest surface area was reported for the catalyst with 25% Fe, corresponding to the catalyst that presented the best activity in the catalytic reaction. Although the reaction under study is a surface reaction, it is clear that the little variation in the surface areas in the fresh and pos-reaction structures (Table 2) indicates that the catalytic activity cannot be fully attributed to surface area variations.

Figure 3A shows the XRD pattern of the $LaCo_{1-x}Fe_xO_3$ phases from x = 0 to x = 1. The end members of the family match with the trigonal ($R\bar{3}c$) and orthorhombic (*Pbnm*)

structures for $LaCoO_3$ and $LaFeO_3$, respectively. The mixed Co/Fe phases in these symmetries display that for x = 0.25 and 0.50, it remained as trigonal ($R\bar{3}c$), whereas, for x = 0.75, it stabilized as orthorhombic (*Pbnm*). This tendency can be observed in Figure 3B, where an enlargement of the main peak area can be observed. To confirm these observations, all patterns were refined with the Rietveld method using the *Fullprof* software. The Rietveld refinements are illustrated in Figure S1 (Supplementary Materials). The unit-cell parameters obtained from Rietveld refinements are listed in Table 3, and the volumes normalized with Z are plotted in Figure S2.
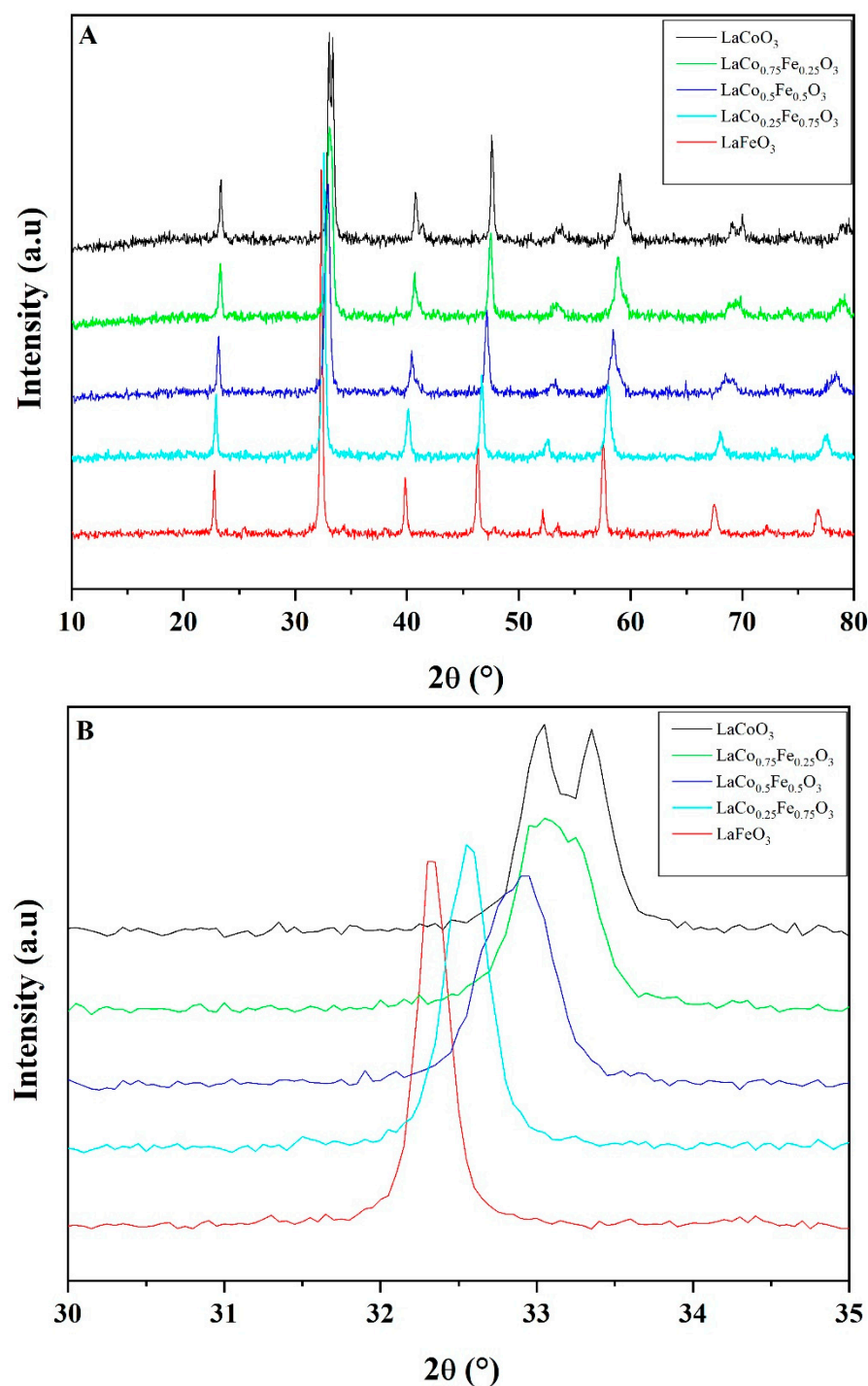

**Figure 3.** (**A**) Diffractograms of the synthesized catalysts. (**B**) Enlargement area of the main peaks.

Table 3. Cell parameters of the synthesized structures.

Catalyst	a (Å)	b (Å)	c (Å)	V (Å^3)
LaCoO$_3$	5.438375	5.438375	13.118483	336.047
LaCo$_{0.75}$Fe$_{0.25}$O$_3$	5.455091	5.455091	13.191200	339.953
LaCo$_{0.5}$Fe$_{0.5}$O$_3$	5.489794	5.489794	13.278933	346.582
LaCo$_{0.25}$Fe$_{0.75}$O$_3$	5.528147	7.799392	5.494007	236.881
LaFeO$_3$	5.553705	5.568998	7.850435	242.803

It can be seen that as the substituted Fe content increased ($0 \leq x \leq 0.5$), the lattice parameters increased, as did the cell volume, which was expected due to the difference in ionic radii (Ri) between Co and Fe: Ri (Co^{2+}) = 0.74 Å, Ri (Co^{3+}) = 0.63 Å, Ri (Fe^{2+}) = 0.76 Å, Ri (Fe^{3+}) = 0.64 Å, and then decreased with a higher degree of substitution ($x = 0.75$) approaching the LaFeO$_3$ value.

The best deactivation resistance of these solids was observed in the LaCo$_{0.75}$Fe$_{0.25}$O$_3$ perovskite, which would indicate that the rhombohedral geometries showed greater stability, maintaining the crystallinity of the solid that only differs from the orthorhombic one due to the coordination distortion of Fe compared to Co [17]. Given that the reducibility of perovskites depends on the crystalline structure, temperature programmed reduction (TPR) tests were also performed to obtain information about the oxidation state of the cations present in the structure. Figure 3 shows the TPR curves of the synthesized perovskites:

The LaCoO$_3$ catalyst presented a reduction profile similar to those reported in the literature for the same phase [18]. The curve presented two main reduction zones, one from 200 °C to 450 °C and the other from 500 °C to 700 °C. The first corresponds to the reduction of Co^{3+} to Co^{2+}, whereas the second is attributed to the reduction of Co^{2+} to Co^0 [19]. As mentioned by Ciambelli et al. [20] and Barbero et al. [21], Fe^{3+} would not be reduced under the experimental conditions of the TPR measurement. In agreement with these results, the green curve in Figure 4 is observed to be completely flattened. Only the reduction of Fe^{4+} to Fe^{3+} would be expected if Fe^{4+} were present.
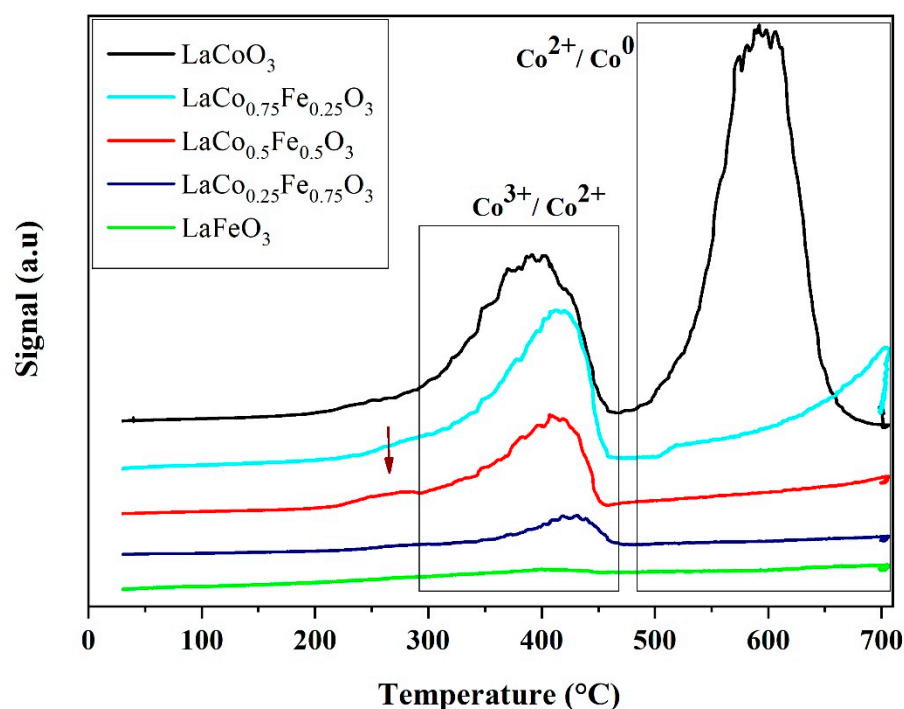
Figure 4. TPR curves of the perovskites.

In general, the reduction temperatures shifted to higher temperatures as the Fe content increased, being the displacement more significant in the reduction of Co^{3+}/Co^{2+} than in the case of Co^{2+}/Co^0, where it is practically observed that the peak of reduction disappears, indicating that the insertion of Fe stabilizes cobalt in its Co^{3+}/Co^{2+} states. This fact could explain the better behavior of the structures containing Fe in the catalytic reaction. The peak at low temperatures could also be assigned to the transition from Fe^{4+} to Fe^{4+}/Fe^{3+}; the second, to Fe^{4+}/Fe^{3+} towards Fe^{3+}. As there is Co in the samples, both peaks would be masked by the reduction of Co^{3+} to Co^{2+}, which also appears in the temperature range from 150 °C to ~450 °C [19]. One peak at ~240 °C is distinguishable in the perovskite with 50% Fe and could indicate the existence of Fe^{4+} for this degree of Co substitution, being masked in the rest of the samples by the greater intensity of the reduction of Co^{3+} to Co^{2+}. The incorporation of Fe affects the first reduction stage, modifying the splitting of the first peak of $LaCoO_3$ perovskite and showing only one peak, probably avoiding an intermediate reduction state. It is also observed that the second reduction peak was displaced at ~600 °C when the Fe content was increased. This peak, which was assigned to the reduction of Co^{2+} to Co^0, decreased in intensity with increasing amounts of Fe and disappeared when the substitution level reached 50%. Furthermore, this peak could also be attributed to the reduction of Fe^{n+} to Fe^0 as it was described by Merino et al. [19], where it was found that this happened when iron was present as free iron oxide outside the perovskite structure. However, the presence of free Fe_2O_3 was ruled out, as pure diffractograms were observed for the perovskite phases obtained. Therefore, only the reduction of Co and a decrease in hydrogen consumption were observed with the increase in iron content, which could indicate the presence of Co^{2+} together with Co^{3+}, as shown in Table 2 (H_2 consumption). Goldwasser et al. [22] stated that perovskite structures are more easily reduced when Fe is replaced by Co. However, in our reaction, the opposite effect was observed. This could explain the fact that the extremes (pure Fe and Co perovskites) did not lead to greater stability in the reaction but that a combined composition of cations gave greater resistance effects that were evidenced in the catalytic stability results. In spite of these partial results, a deeper study of the oxidation states of iron and cobalt is essential to know the physicochemical reasons for the high stability of the catalyst. Therefore, Mössbauer and X-ray photoelectronic spectroscopies were used to analyze the redox behavior. Figure 5 shows the Mössbauer spectra at 298 K and 12 K of the four perovskites with iron. The spectrum corresponding to $LaFeO_3$ presents a sextet with narrow absorption peaks and a horizontal baseline. These aspects are typical of a solid with magnetic ordering; $LaFeO_3$ is antiferromagnetically ordered below $\cong$ 477 °C, without magnetic relaxation and with environments of Fe ions very similar to each other. The hyperfine parameters obtained from the fitting are presented in Tables 4 and 5. These correspond to Fe^{3+} ions octahedrally coordinated with a high spin configuration, and they are very similar to those previously reported by other authors for $LaFeO_3$ [23,24]. The value of the quadrupole shift (2ε), nearly equal to zero, indicates that the octahedral environment is highly symmetric. In addition, a central signal (δ = 0.3 mm/s) with a contribution of 1–2% is detected, which could be assigned to a Fe^{3+} paramagnetic impurity not detected by XRD due to its low concentration.
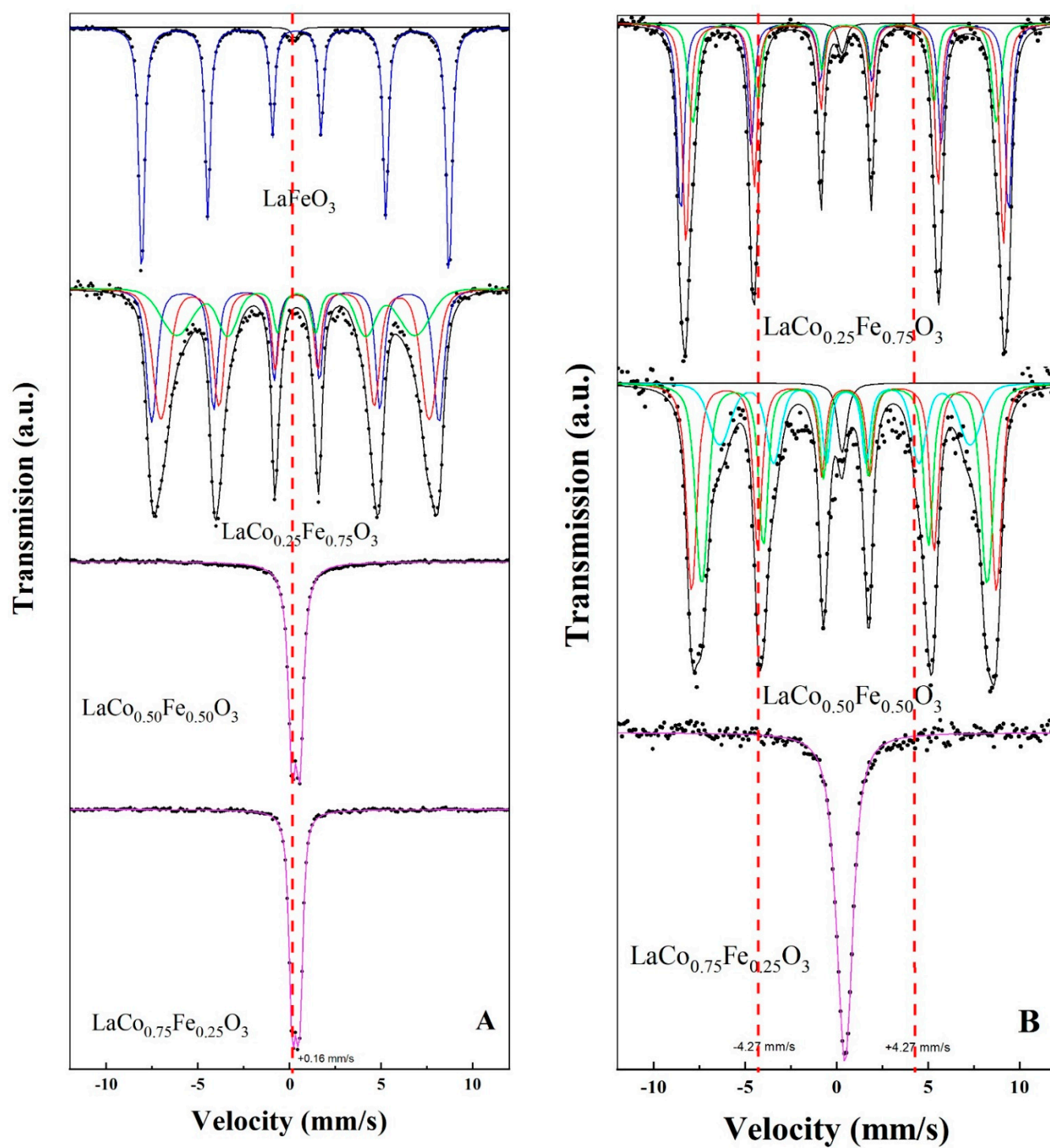
Figure 5. Mössbauer spectra: (**A**) at 298 K and (**B**) at 12 K.

Table 4. Hyperfine Mössbauer parameters of $LaFeO_3$, $LaCo_{0.25}Fe_{0.75}O_3$, $LaCo_{0.5}Fe_{0.5}O_3$, and $LaCo_{0.75}Fe_{0.25}O_3$ at 298 K.

Species	Parameters	$LaFeO_3$	$LaCo_{0.25}Fe_{0.75}O_3$	$LaCo_{0.5}Fe_{0.5}O_3$	$LaCo_{0.75}Fe_{0.25}O_3$
$P_{site}(0)$ (blue Interaction)	H (kOe)	520.4 ± 0.1	486.1 ± 0.9	——	——
	δ (mm/s)	0.36 ± 0.01	0.36 ± 0.01	——	——
	2ε (mm/s)	-0.07 ± 0.01	-0.09 ± 0.01	——	——
	%	99 ± 1	33 ± 2	——	——
$P_{site}(1)$ (red Interaction)	H (kOe)	——	454 ± 3	——	——
	δ (mm/s)	——	0.35 ± 0.01	——	——
	2ε (mm/s)	——	-0.08 ± 0.02	——	——
	%	——	41 ± 3	——	——
$P_{site}(2)$ (green Interaction)	H (kOe)	——	403 ± 8	——	——
	δ (mm/s)	——	0.37 ± 0.03	——	——
	2ε (mm/s)	——	-0.05 ± 0.06	——	——
	%	——	26 ± 3	——	——
Magnetic relaxing (violet Interaction)	Δ (mm/s)	——	——	0.43 ± 0.01	0.38 ± 0.01
	δ (mm/s)	——	——	0.35 ± 0.01	0.34 ± 0.01
	%	——	——	100	100
Paramagnetic contaminant (black Interaction)	δ (mm/s)	0.3 *	——	——	——
	%	1 ± 1	——	——	——

$P_{site}(i)$: probability to have Fe^{3+} ions with "i" Co ions as neighbors. H: hyperfine magnetic field; δ: isomer shift (all the isomer shifts are referred to α-Fe at 298 K); 2ε: quadrupole shift; Δ: quadrupole splitting. (*): parameter held fixed in fitting.

Table 5. Hyperfine Mössbauer parameters of $LaFeO_3$, $LaCo_{0.25}Fe_{0.75}O_3$, $LaCo_{0.5}Fe_{0.5}O_3$, and $LaCo_{0.75}Fe_{0.25}O_3$ at 12 K.

Species	Parameters	$LaCo_{0.25}Fe_{0.75}O_3$	$LaCo_{0.5}Fe_{0.5}O_3$	$LaCo_{0.75}Fe_{0.25}O_3$
$P_{site}(0)$ (blue Interaction)	H (kOe)	556 ± 1	——	——
	δ (mm/s)	0.47 ± 0.01	——	——
	2ε (mm/s)	-0.08 ± 0.02	——	——
	%	33 ± 3	——	——
$P_{site}(1)$ (red Interaction)	H (kOe)	538 ± 1	517 ± 2	——
	δ (mm/s)	0.47 ± 0.01	0.45 ± 0.02	——
	2ε (mm/s)	-0.08 ± 0.01	-0.10 ± 0.03	——
	%	42 ± 3	36 ± 3	——
$P_{site}(2)$ (green Interaction)	H (kOe)	515 ± 2	484 ± 3	——
	δ (mm/s)	0.46 ± 0.01	0.46 ± 0.02	——
	2ε (mm/s)	-0.08 ± 0.03	-0.08 ± 0.03	——
	%	23 ± 2	38 ± 3	——
$P_{site}(3)$ (magenta Interaction)	H (kOe)	——	425 ± 7	——
	δ (mm/s)	——	0.49 ± 0.05	——
	2ε (mm/s)	——	-0.1 ± 0.1	——
	%	——	24 ± 2	——
Magnetic relaxing (violet interaction)	H (kOe)	——	——	399 ± 14
	δ (mm/s)	——	——	0.41 ± 0.02
	2ε (mm/s)	——	——	-0.06 ± 0.04
	%	——	——	100
Paramagnetic contaminant (black interaction)	δ (mm/s)	0.3 *	0.3 *	——
	%	2 ± 1	3 ± 1	——

$P_{site}(i)$: probability to have Fe^{3+} ions with "i" Co ions as neighbors. H: hyperfine magnetic field; δ: isomer shift (all the isomer shifts are referred to α-Fe at 298 K); 2ε: quadrupole shift. (*): parameter held fixed in fitting.

Replacing 25% Fe with Co produces a significant change in the spectrum: the peaks broaden considerably and the baseline curves. This behavior indicates that the Fe^{3+} ions have different environments and that the system undergoes magnetic relaxation phenomena. The change is drastic for the other two compositions, where a complete collapse of the magnetic ordering occurs. Magnetic relaxation can occur by superparamagnetism phenomena or by spin–spin or spin–lattice relaxation. Superparamagnetism manifests itself when the size of the particles is very small, in the nanometer range. In these samples, this

effect could be neglected taking into account that they have been calcined at 750 °C and that the XRD diagrams show narrow lines. For this reason, the results can be attributed to modifications in the spin–spin or spin–lattice relaxation modes caused by the replacement of Fe by Co.

The spectra were measured again at 12 K to go below the temperature region where spin dynamics occur and thus to obtain more information. In Figure 5B, it can be seen that $LaCo_{0.25}Fe_{0.75}O_3$ presents a complete magnetic blocking at this temperature; $LaCo_{0.5}Fe_{0.5}O_3$ still undergoes relaxation phenomena (curved background), whereas $LaCo_{0.75}Fe_{0.25}O_3$ starts to experience the beginning of a magnetic blocking. A similar qualitative effect was reported by Berry et al. for $LaCo_{0.5}Fe_{0.5}O_3$ and $LaCo_{0.90}Fe_{0.10}O_3$ [25] and by Troyanchuk et al. for $LaCo_{0.9}Fe_{0.1}O_3$ and $LaCo_{0.6}Fe_{0.4}O_3$ [26]. In both cases, the mixed perovskites were obtained by the ceramic method.

In principle, three sextets could be detected in each mixed perovskite. However, in the case of $LaCo_{0.75}Fe_{0.25}O_3$, the magnetic relaxation phenomena prevent this detection even at a temperature as low as 12 K. Another aspect to mention is that the tendency in the structures with lower Fe concentrations causes the hyperfine magnetic field to strongly decrease, and the width of the distribution of this parameter increases, indicating the presence of an increasing number of environments with slightly different symmetries.

The $LaFeO_3$ perovskite has a relatively high antiferromagnetic ordering temperature ($T_{Neel} \cong 477$ °C), which shows very strong exchange interactions between the high-spin Fe^{3+} ions. This is reflected in the narrow line sextet of the Mössbauer spectrum obtained at 298 K and shown in Figure 5A. The changes described as a consequence of the increasing substitution of Fe ions by Co ions (appearance of magnetic relaxation phenomena that culminate in the total collapse of the ordering when the substitution reaches 75%, even at a temperature as low as 12 K) indicate that Co causes a very strong dilution of the magnetic interactions among Fe^{3+} ions.

Co is found as Co^{3+} and/or Co^{2+} and is located in highly symmetrical octahedral sites surrounded by six oxygen anions. Under these conditions, the possible electronic configurations that it could adopt are:

Co^{3+}:
- high spin: $t_{2g}{}^4 e_g{}^2$
- intermediate spin: $t_{2g}{}^5 e_g{}^1$
- low spin: $t_{2g}{}^6 e_g{}^0$

Co^{2+}:
- high spin: $t_{2g}{}^3 e_g{}^2$
- intermediate spin: $t_{2g}{}^4 e_g{}^1$
- low spin: $t_{2g}{}^5 e_g{}^0$

If for each configuration the corresponding magnetic moment is calculated assuming, in a first approximation, that only the spin magnetic moment is considered: $\mu_s = (n(n + 2))^{0.5} \mu_B$, (where n is the number of unpaired electrons), the following values are obtained:

Based on this analysis, the drastic effect on the magnetic order produced by the substitution of Fe^{3+} by Co would be justified if the latter were found as Co^{3+} in a low-spin configuration. Other authors have reached similar conclusions for the $LaCo_{1-x}Fe_xO_{3-d}$ system [30]. Recently, a similar effect has been reported when substituting high-spin Fe^{3+} for low-spin Co^{3+} on the magnetic properties of α-Fe_2O_3, which also presents an antiferromagnetic ordering [27].

From these results, it can be inferred that if small amounts of Co^{2+} are present surely these ions would have a low spin configuration, as it is the one with the lowest magnetic moment. Due to the existence of Co^{2+}, the electroneutrality of the system can be preserved by the appearance of oxygen vacancies or by the emergence of abnormally high oxidation states of Fe (Fe^{4+}). It is now accepted that if Fe^{4+} is present in the sample when the temperature is lowered, it undergoes the following disproportionation reaction [28].

$$2Fe^{4+} \rightarrow Fe^{3+} + Fe^{5+}$$
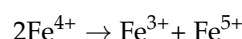
Fe^{5+} produces a sextuplet whose hyperfine parameters are: H = 265 kG, $\delta \cong 0$ mm/s, and $\varepsilon \cong 0$ mm/s [29]. This implies that the two most intense peaks of the sextet (peaks 1 and 6) should appear at -4.27 and $+4.27$ mm/s, respectively (their position is indicated in the 12 K spectra with a red dotted line). Evidently, for $LaFe_{0.75}Co_{0.25}O_3$, the line at $+4.27$ mm/s is not recorded (a "valley" appears in the spectrum in this region). The line at -4.27 mm/s could be hidden by the line "2" of the Fe^{3+} signals. However, if this was the case, the envelope corresponding to those lines should be more intense than the envelope of line "5", which is not the case. Therefore, the presence of Fe^{5+} can be ruled out in this sample. Corroborating this conclusion, the characteristic Fe^{4+} singlet at $\delta \cong 0.16$ mm/s is not recorded in the spectrum at room temperature (its position is indicated by a red dotted line in the spectrum at 298 K).

In the case of $LaFe_{0.5}Co_{0.5}O_3$, although the situation is not as clear as with the previous sample, once again, the presence of the -4.27 mm/s line should generate an asymmetry in the envelope of line "2" with respect to line "5" that is not recorded. Similarly, at 298 K, the existence of an Fe^{4+} singlet would produce an asymmetry in the central doublet, with the peak on the left being more intense than the one on the right. Therefore, it could also be concluded that there is no charge compensation due to an increase in the oxidation state of Fe ions. In the case of $LaFe_{0.25}Co_{0.75}O_3$, magnetic relaxation phenomena prevent obtaining this type of conclusion. With this technique, it is possible to study the oxidation states in the bulk, which is why XPS was also carried out to identify the oxidation states on the catalysts' surface. Figures 6–8 show the results for Co2*p*, Fe2*p*, and O*1s*, and Table 6 shows the main data extracted from these graphs.
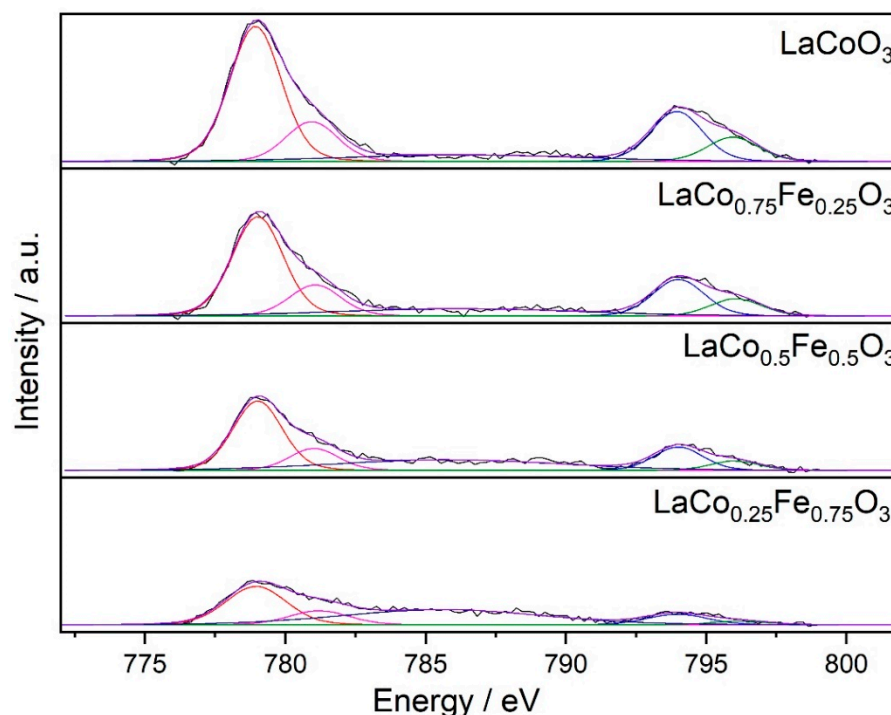

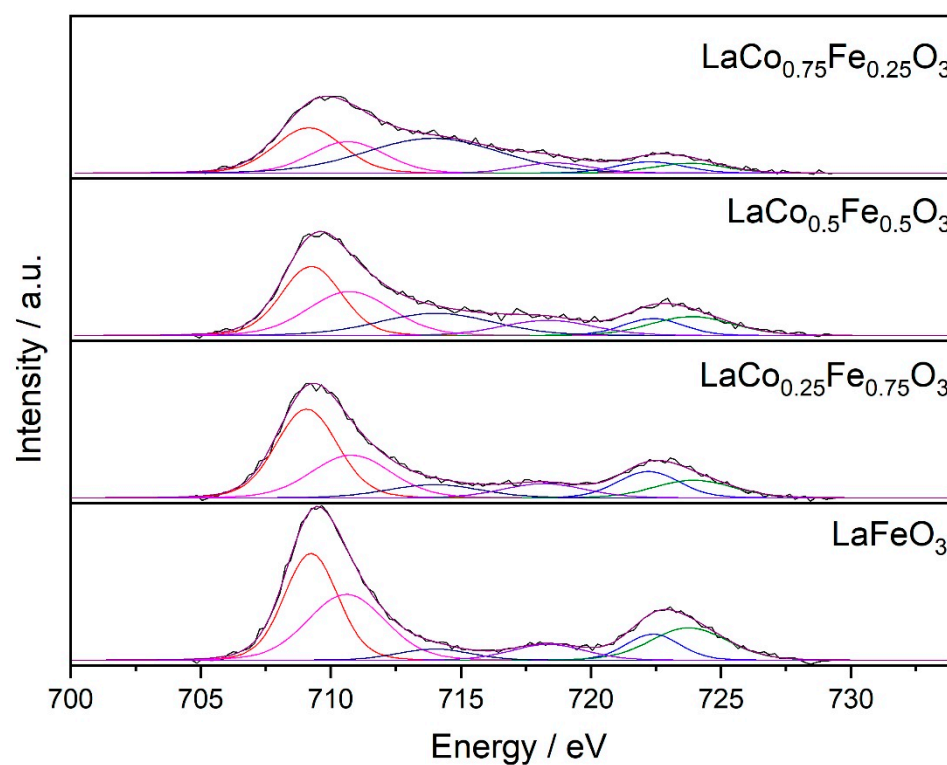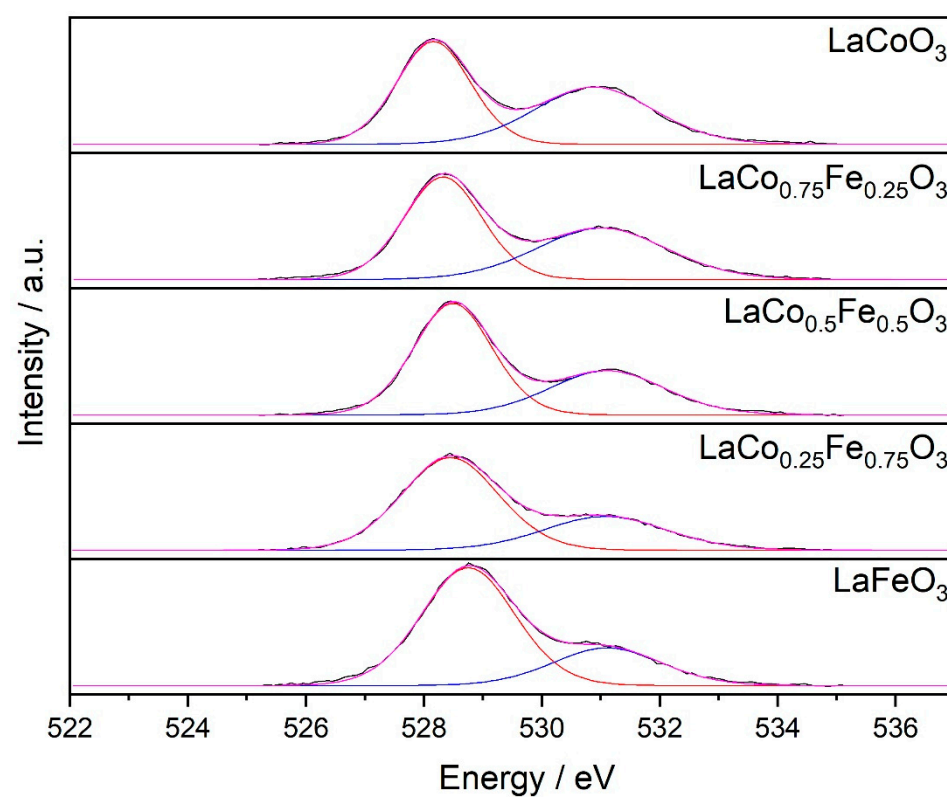**Figure 6.** XPS spectra of Co2*p*.

Figure 7. XPS spectra of Fe2p.

Figure 8. XPS spectra of O1s.

Table 6. Co^{3+}/Co^{2+} magnetic moments.

Oxidation State	Magnetic Moment, μ_B		
	High Spin	**Intermediate Spin**	**Low Spin**
Co^{3+}	4.90	2.83	0
Co^{2+}	5.92	3.87	1.73

Figure 6 shows the XPS spectrum of the Co2*p* signal. The Co2$p_{3/2}$ peak can be deconvoluted into two components, at 778 and 781 eV, assignable to the Co2p and Co3p surface species, respectively, whereas the peak around 793.5 eV, which corresponds to Co2$p_{1/2}$, can also be deconvoluted into two peaks due to the existence of these two cobalt species. Between 785–790 eV it is possible to appreciate that as Fe substitution increased, the intensity of a satellite peak in that region increased, showing that the structure is ordered in such a way that both Co species and Fe species coexist. Specifically, in the case of the XPS spectra of Co, this peak indicates the existence of Co^{2+} as it was described by Wang et al. [30]. The analysis of the results shows, as expected, a decrease in the Co signals as the Fe content increases. In addition, from Figure 6, it can be observed how the relative intensity of the satellite peak around 785–790 eV increases with respect to the other Co signals. As already discussed, this positively influences the catalytic reaction considering that this decrease could interfere in the oxidation-reduction process and would cause greater durability of the structure. In addition, the presence of the species that are detected by this technique promotes active oxygen vacancies during the reaction, accelerating the combustion process [31].

The highest Co^{2+}/Co^{3+} ratio occurs with the lowest and highest percentages of Fe substitution, while the highest Fe^{3+}/Fe^{2+} atomic ratios were obtained in structures with 50% and 100% substitution. However, analyzing Table 7 as a whole, it is possible to conclude that an intermediate percentage of substitution yields a greater energy difference between the Co2*p(1/2)* and Co2*p(3/2)* peaks, evidencing the presence of both Co species. These species would present greater participation in the catalytic activity [18,30]. Figure 7 shows an intense peak around 710.5 eV, corresponding to Fe2$p_{3/2}$ that deconvolves into two possible peaks attributed to Fe^{3+} and Fe^{2+}, which are the most stable states in which this metal can be found in the structure. At higher binding energies, an intense peak around 722.9 eV is also observed, which corresponds to Fe2$p_{1/2}$, which also deconvolves into two possible peaks that are masked by its width and which, like the first peak, can be attributed to the coexistence of Fe^{3+} and Fe^{2+}. In the region between 715–721 eV, satellite peaks are observed that correspond to the coexistence of both Fe oxidation states, and also to the possible appearance of metallic Fe in the structure [32]. The presence of metallic Fe is unlikely in these working conditions. However, it is not possible to rule out the existence of this species that could justify the deactivation of the catalysts by the inactivation of the cations of this metal. As described, the coexistence of different Fe cations is inferred from these results due to the reduction of this species in the perovskite structure, which can influence the catalytic reaction depending on the effect on the rest of the cations that play a fundamental role in the reaction under study.

Table 7. XPS results.

Catalyst	O_{ads}/O_{latt}	Co^{2+}/Co^{3+}	Fe^{3+}/Fe^{2+}	Energy Difference (eV) between Co2*p(1/2)* and Co2*p(3/2)* XPS Signals
$LaCoO_3$	0.93	0.31	——	15.18
$LaCo_{0.75}Fe_{0.25}O_3$	0.87	0.36	0.81	15.29
$LaCo_{0.5}Fe_{0.5}O_3$	0.60	0.34	1.06	15.08
$LaCo_{0.5}Fe_{0.5}O_3$	0.48	0.36	0.72	14.76
$LaFeO_3$	0.39	——	1.16	——

As noted above, as Fe is incorporated into the structure, surface sites of Co2p are replaced by Fe, and the relative intensity of the satellite peak between 785–790 eV increases with respect to the other Co signals, indicating the presence of Co^{2+}. This is in correspondence with what was observed for Fe, where the analysis of the results shows an increase in the Fe signals as the Fe content increases. In addition, Figure 7 shows that the relative intensity of the satellite peak (715–720 eV) increases with Fe content, indicating the coexistence of iron in its 2+ and 3+ states.

The XPS spectra of O*1s* shown in Figure 8 reflect two intense peaks between 528–533 eV, clearly demonstrating the existence of two oxygen species on the surface. The peak with the highest binding energy (530.9–531.2 eV) corresponds to surface oxygens (O_{ads}) such as O_2^{2-} or O^- and $(OH)^-$ hydroxyl anion, while the peak at low binding energies (528.1–528.8 eV) is attributed to O^{2-}, oxygens of the lattice (O_{latt}) [33].

As the amount of Fe in the structure increases, it can be observed that the most intense peak of O1s spectra shifts to higher energies, whereas the less intense one undergoes practically imperceptible changes. Modifications were also observed in the O_{ads}/O_{latt} ratio (Table 6), which decreased while the Fe content in the structure increased.

This decrease can also be explained by the cationic ordering on the surface that competes with the different oxygen species that occupy these sites. The O_{ads}/O_{latt} ratio is a measure of surface oxygen vacancies that has a marked influence on the oxidation reactions. The highest ratio is not in line with the increase in Fe in the structure, but with an amount of 25% Fe, the O_{ads}/O_{latt} ratio is the highest in the mixed perovskites, and therefore this could also explain the higher catalytic activity of this catalyst.

Mössbauer spectroscopy and XPS results confirmed that to the extent of the greater substitution of Fe, the cationic environment of Co increased to a point where the presence of Fe became more significant, that is, up to 25% of the insertion of Fe. With a greater percentage of substitution, the structure collapsed its magnetic ordering. The different environments of Fe^{3+} varied with increasing substitution and produced changes that influenced the stability of the material in the combustion reaction. With a 25% substitution of Fe, the structure is magnetically and electronically balanced, causing greater resistance during the oxidation process. Based on the redox mechanisms discussed, it is important to analyze the capacity and possible mobility of oxygen in the structure. Thus, an O_2-TPD study was carried out, and the results are shown in Figure 9.

As shown in Figure 9, it is possible to differentiate two species of oxygen in the structure: α or surface oxygens that desorb between 200 °C and 400 °C, and β or lattice oxygens that desorb between 500 °C and 800 °C [34]. The limited amount of surface oxygen is noticeable except in the LaFeO$_3$ sample. This can be explained assuming that the vacancies on the surface are occupied by the combination of the Fe^{3+}/Co^{3+} cations, leaving the possibility of dynamic exchange between O_{ads}/O_{latt}, which is observed and corroborated by the atomic relationships determined by XPS (Table 7). The lowest O_{ads}/O_{latt} ratio is obtained for the LaFeO$_3$ perovskite, whereas the highest ratios are obtained for the LaCoO$_3$ and LaCo$_{0.75}$Fe$_{0.25}$O$_3$ structures. It is well known that the catalytic combustion process of CVOCs mainly includes breaking the C–C bond (346 kJ mol^{-1}), C–H bond (411 kJ mol^{-1}), and C–Cl bond (327 kJ mol^{-1}). Thermodynamically, the bond energy of the C–Cl bond is lower, so it is easier to break. Chlorobenzene is generally adsorbed and dissociated on surface active sites via a nucleophilic attack on C–Cl bond. Then, the adsorbed species react with active oxygen species to produce CO_2 and H_2O. Simultaneously, the dissociative Cl^- species adsorbed are oxidized into Cl_2 by the surface reactive oxygen species through the Deacon reaction ($2HCl + O_2 \rightarrow Cl_2 + H_2O$). Finally, the consumed oxygen species are replenished by the gas-phase oxygen adsorbed on the oxygen vacancies [35,36]. Thus, the lattice oxygens play a fundamental role, and that is why the best catalytic behavior corresponds to the highest O_{ads}/O_{latt} ratio that occurs in the LaFe$_{0.25}$Co$_{0.75}$O$_3$ structure. There is a correspondence between what is observed in Figure 8 with this O_{ads}/O_{latt} ratio, which is why it is justified that the occupancy of the active sites and the amounts of Co ions, which are affected by the insertion of Fe, have important roles in the activity and stability of the catalyst.
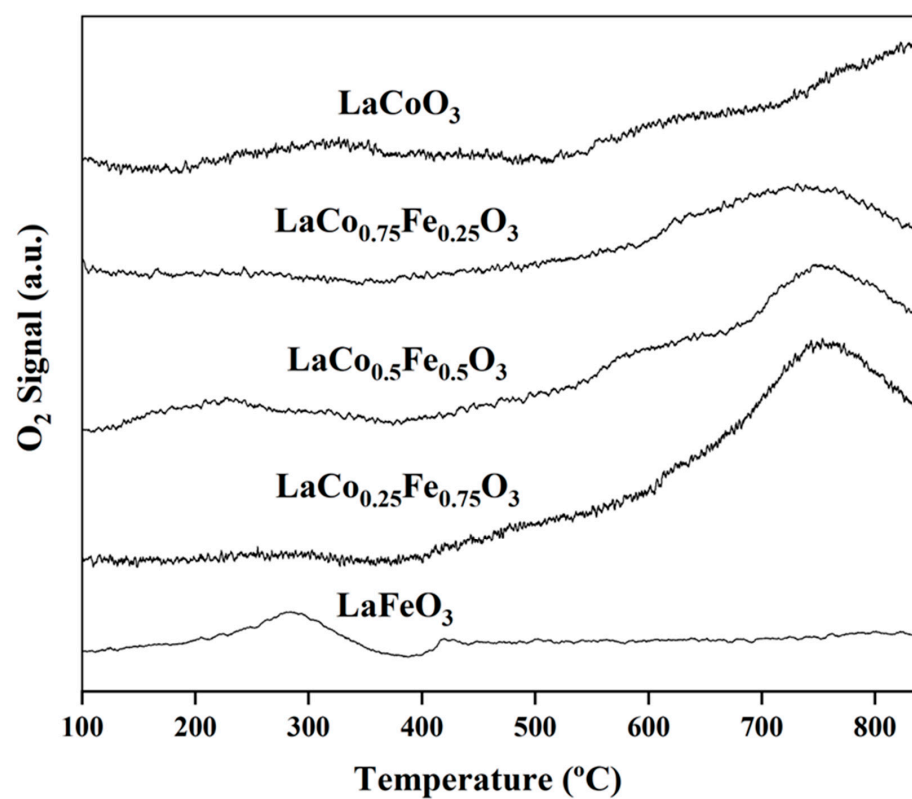
Figure 9. O_2-TPD curves of the catalysts.

2.3. Pos-Reaction Analysis

To determine the possible causes of catalyst deactivation, pos-reaction samples were characterized by XRD, XPS, and S_{BET} after being evaluated in the chlorobenzene oxidation reaction. Figure 10 shows the diffractograms of the used catalysts.
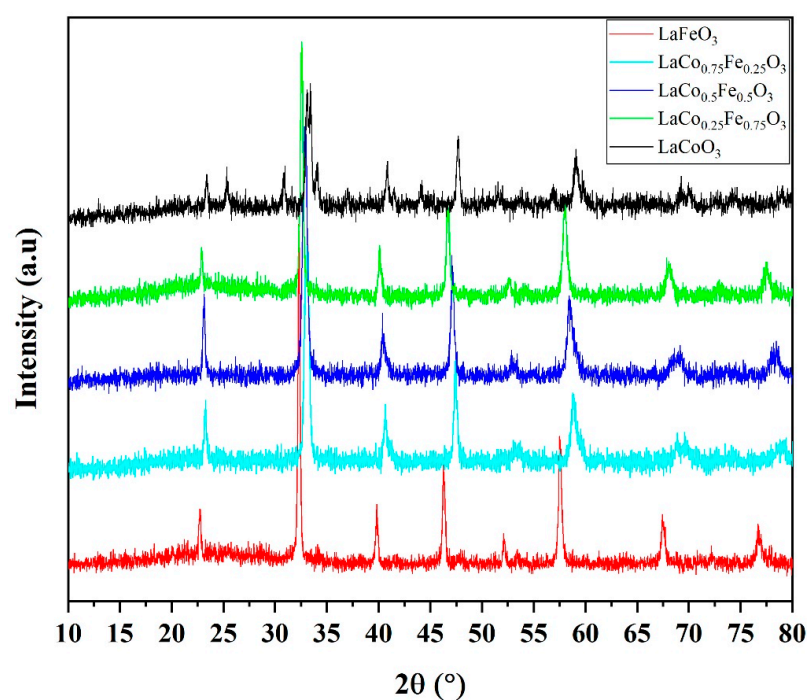

Figure 10. XRD patterns of the post-reaction catalysts.

No modifications of the structure were detected by XRD. The samples maintained the main peaks of the structures before the reaction, with the exception of the $LaCoO_3$ catalyst, where a destruction of the structure is observed as the main peak of the perovskite is modified. There are three additional peaks that correspond to the appearance of the LaOCl phase (PDF 96-900-9171), a modification that has been discussed in previous works [12] and attributed to the absorption of Cl species on the catalyst surface, a situation that in the case of the Fe-containing catalysts did not happen. Table 2 presents specific surface areas of fresh and used catalysts. It can be highlighted that there are no marked differences between values. In the case of $LaCoO_3$ and $LaCo_{0.75}Fe_{0.25}O_3$, a small surface area difference of about two units was observed. However, marked differences in pore size and volume can be seen, in all cases attributable to the surface reaction. As was previously mentioned, the $LaCoO_3$ catalyst is the one that formed the least amount of Cl_2 after the catalytic reaction (see Table 1) in line with what is observed in Figure 10. Part of the Cl_2 reaction product remained adsorbed on the catalyst surface, destroying the perovskite structure to form LaOCl.

XPS studies of pos-reaction samples evidenced the presence of Cl on the surface of all catalysts. In the case of perovskites with Fe, the variations in the stability time of the structures and their deactivation could also be associated with the adsorption of Cl on the surface. Although this was not perceptible by XRD due to the low concentration of this species, it was possible to identify the presence of this product as it is shown in Figure 11.
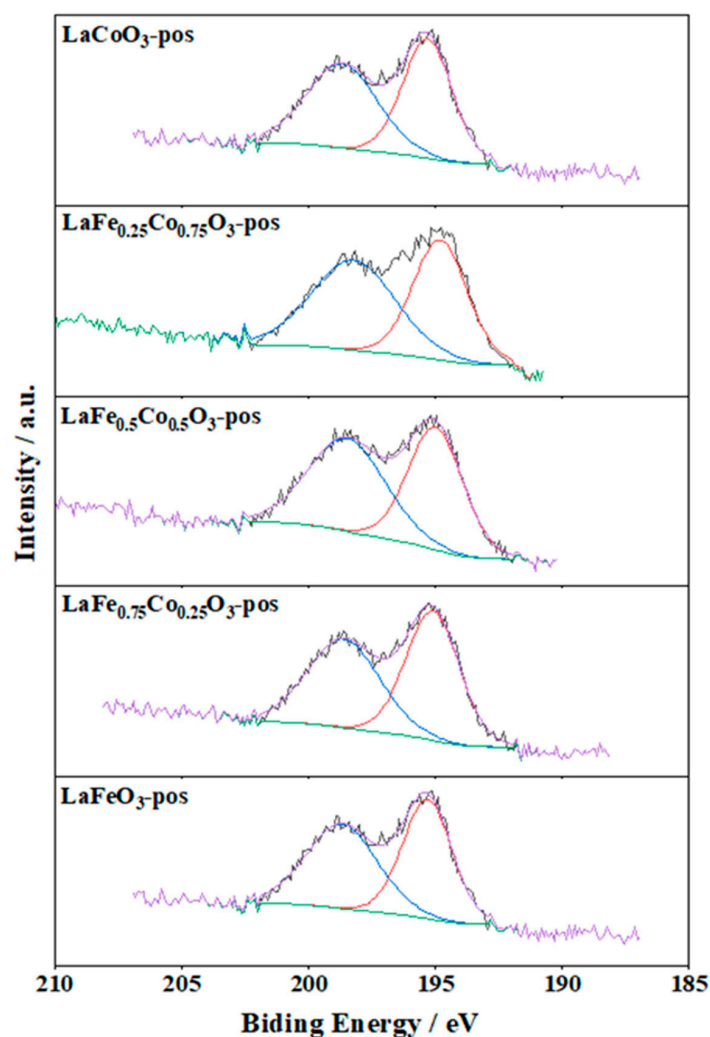

Figure 11. Cl2p XPS spectra of pos-reaction catalysts.

Two signals can be observed in Figure 11, one corresponding to $Cl2p_{1/2}$ around 195 eV and the other around 199 eV corresponding to $Cl2p_{3/2}$. Both signals suggest the presence of the Cl^- ion related to the structure in different ways. As described by Bello et al. [37], one of the ways in which this ion can be found is bounded to oxygen bounded to one of the metals of the solid (Metal–O–Cl), which is in line with the results observed in the present work. Atomic ratios determined by XPS of the used samples (Table 8) showed that the highest proportion of Cl appears in the $LaCoO_3$ catalyst, a structure that is destroyed by the formation of LaOCl, as was observed by the XRD diffractograms. Another way in which this ion can be associated with the structure is directly linked to a metal (Metal–Cl), a relationship that was not found as the formation of any metal chloride was not detected by the techniques used, maybe because the thermodynamic conditions are not favorable for the appearance of these structures or due to the low concentration of this species. From these results, it can be ensured that the deactivation of the catalysts happened due to the surface adsorption of Cl, which can occur both in oxygen vacancies or in some active sites on the surface, in both cases causing lower stability of the catalyst [38].

Table 8. XPS pos-reaction results.

Catalyst	O_{ads}/O_{latt}	Co^{2+}/Co^{3+}	Fe^{3+}/Fe^{2+}	$Cl/(Co + Fe + O)$
$LaCoO_3$	0.43	0.28	——	0.23
$LaCo_{0.75}Fe_{0.25}O_3$	0.69	0.31	0.77	0.16
$LaCo_{0.5}Fe_{0.5}O_3$	0.46	0.40	0.95	0.21
$LaCo_{0.25}Fe_{0.75}O_3$	0.40	0.42	0.69	0.20
$LaFeO_3$	0.31	——	0.98	0.20

Comparing Figures 6 and 12, it can be concluded that the Co^{2+}/Co^{3+} ratio decreases once the catalyst is used, with the exception of the $LaCo_{0.75}Fe_{0.25}O_3$ catalyst, which presented the same intensity peak. There were no notable changes for the $LaCoO_3$ and $LaCo_{0.75}Fe_{0.25}O_3$ catalysts in the case of the satellite peak between 785–790 eV. On the contrary, for $LaCo_{0.25}Fe_{0.75}O_3$ and $LaCo_{0.5}Fe_{0.5}O_3$, an increase in intensity is observed, evidencing a greater presence of Co^{2+}. The modification in the intensity of this peak suggests a change in the oxidation state that can be related to chlorine adsorption on the surface. These variations can be observed by comparing Figure 6 with data in Tables 7 and 8.
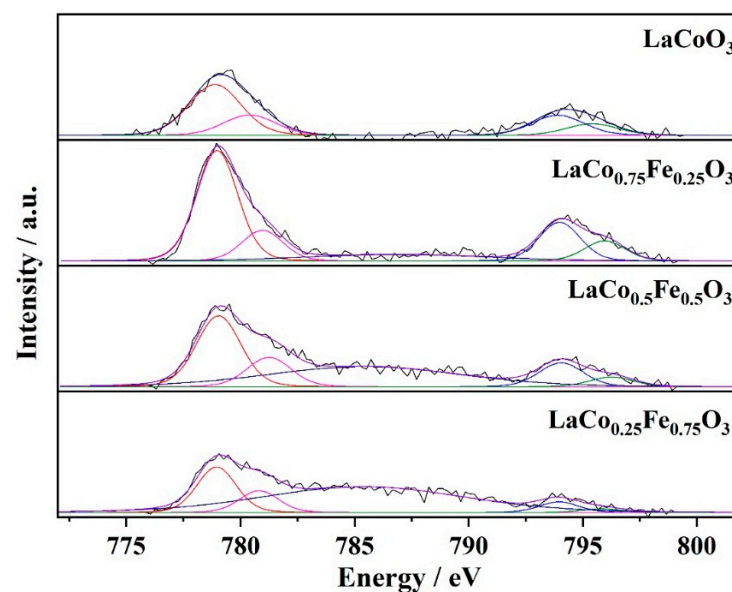

Figure 12. XPS spectra of Co2p post-reaction.

If Figures 7 and 13 are compared, it can be observed that the Fe^{3+}/Fe^{2+} ratio decreases for the used catalysts. It is possible that the behavior of the redox couple and the disposition of the cations were modified when the Cl occupied sites on the surface that were interchangeable in the case of the fresh catalyst. Once the Cl adsorbs to the surface, the states and dispositions of the cations suffer alterations in terms of oxidation state and spatial arrangement, which are clearly reflected in Table 7.
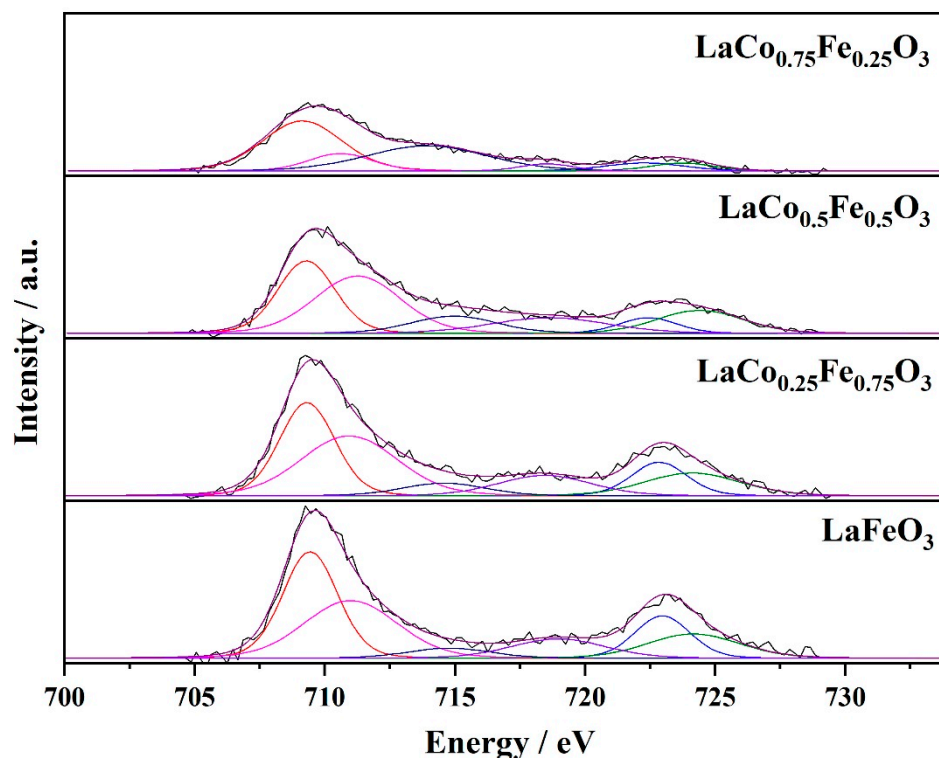
Figure 13. XPS spectra of Fe2p post-reaction.

In the region of 528–533 eV (Figure 13), an intense peak that corresponds to the oxygens of the lattice is observed. Comparing Figures 8 and 14, it is observed that the Oads/Olatt ratio decreases in all cases. This result is consistent with that obtained in the catalytic reaction, considering that combustion requires a constant exchange of different oxygen species. The bonding of chlorine on the surface affects the occupancy of oxygen on the surface, and it avoids the exchange between the oxygens of the lattice and the superficial ones, inhibiting the catalytic activity, which is why the greatest stability is seen in the catalyst with the highest Oads/Olatt ratio.

Based on the previous analyses, it could be concluded that in mixed perovskites, at least in $LaCo_{0.75}Fe_{0.25}O_3$, charge compensation is produced by the generation of oxygen vacancies, attributable to the existence of Co^{2+} facilitated by the different Fe cations in the structure. The analysis of the magnetic environments, the possible oxidation states of Fe, and the pos-reaction results is in perfect agreement with the best behavior of this catalyst in the catalytic reaction, supporting up to 100 h of time on stream without modifying its original structure. This demonstrates the high stability that Fe in low concentrations provides to the $LaCoO_3$ perovskite.
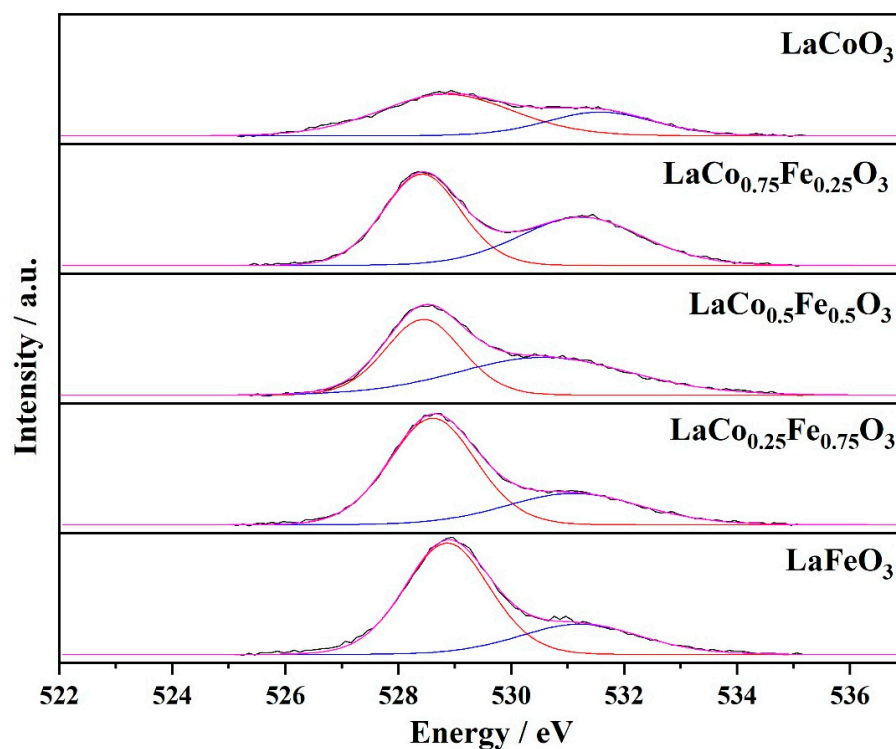
Figure 14. XPS spectra of O1s post-reaction.

3. Experimental

3.1. Catalyst Synthesis

A $LaCo_{1-x}Fe_xO_3$ (x = 0; 0.25; 0.5; 0.75; 1) series was synthesized by the citrate method, using stoichiometric quantities of $La(NO_3)_3$, $Co(NO_3)_2$, and $Fe(NO_3)_3$, and 10% citric acid as a binder, (Merck, Burlington, Canada). The nitrates were dissolved separately in the minimum quantity of distilled water, stirring for approximately 5 min. Once translucent solutions were obtained, it was mixed with the citric acid solution. This mixture was kept stirring for 10 min. Afterwards, the resulting solution was concentrated, and the water evaporated under vacuum in a rotary evaporator at 75 °C until a translucent and viscous gel was obtained. This gel was transferred to a crystallizer to dry in a vacuum oven at an initial temperature of 75 °C and gradually increased until reaching 100 °C, the temperature at which it was kept drying between 12–15 h in order to obtain an amorphous solid precursor. The resulting solid was ground until obtaining a very fine powder that was then calcined in an air atmosphere with a temperature ramp of 2.5 °C/min from 30 °C to 400 °C, the temperature at which was kept for half an hour, and then increased up to 700 °C for 2 h. In all cases, the stoichiometric amounts were calculated to obtain 4 g of catalysts.

3.2. X-ray Diffraction (XRD)

X-ray diffraction (XRD) was performed in continuous mode with 2θ angles between 10 and 80° at a rate of 3°/min with a step of 0.02. The analysis was performed in a Rigaku Ultima IV model equipment (Rigaku Company, Tokyo, Shibuya, Japón) with a Cu lamp ($\lambda_{CuK\alpha1}$ = 1.54056 Å, $\lambda_{CuK\alpha2}$ = 1.54440 Å). The patterns obtained were refined by applying the Rietveld method [39] using the Fullprof program [40].

3.3. BET Surface Area

The specific surface area (S_{BET}) of the synthesized catalysts was analyzed in a GEMINI V2.00 Micrometrics Instrument equipment (Norcross, GA, United States) the adsorption isotherm with nitrogen at 77 K. Initially, the samples were degassed for 12 h at 250 °C, and between 250 mg and 500 mg of catalyst were used in all cases.

3.4. Temperature Programmed Reduction (TPR)

Temperature programmed reduction (TPR) analyses were performed in a homemade U-shaped quartz tubular reactor using a TCD detector and a catalyst mass between 100 and 250 mg. A 5% H_2/N_2 mixture with a total flow of 30 mL min^{-1} was used as a reducing gas. The temperature was increased from room temperature at a rate of 10 °C min^{-1} up to 700 °C.

3.5. Temperature Programmed Desorption of Oxygen (O$_2$-TPD)

Temperature programmed desorption of oxygen (O_2-TPD) experiments were performed using the same equipment as for TPR, this time coupled to an Ametek Dycor Dymaxion mass spectrometer (PerkinElmer company from Cleveland, OH, USA). First, cleaning of the sample surface of the catalyst (150 mg) was carried out in Ar flow, from room temperature to 700 °C at a rate of 10 °C min^{-1}. The sample was then cooled to 400 °C, at which point, a 20% O_2/Ar current was fed. The adsorption was reached at 400 °C for 30 min. Then, the reactor temperature was decreased, subsequently purged with pure Ar for 30 min, and finally heated to 950 °C with a ramp of 10 °C min^{-1}, where it was maintained for 30 min. Simultaneously, the desorbed oxygen signal at m/z = 32 was recorded by the mass spectrometer.

3.6. X-ray Photoelectron Spectrometry (XPS)

X-ray photoelectron spectra were collected using a VG Microtech ESCA 2000 spectrometer (Halifax, Nueva Escocia, Canadá) with a non-monochromatic Al Kα radiation source (300 W, 15 kV, hν = 1486.6 eV), combined with a 100-AX VG-hemispherical analyzer, operating at a step energy of 25 eV. The resolution of the instrument was 0.1 eV. All binding energies (BE) were referred to the C1s peak at 284.8 eV, to correct for possible spectral shifts due to charging effects. The chamber pressure was maintained at $< 10^{-9}$ Torr during all the measurements.

3.7. Mössbauer Spectrometry

Mössbauer spectra were obtained in transmission geometry using a 512-channel constant-acceleration spectrometer (WissEl, Starnberg, Germany), equipped with a ^{57}Co source in a nominal 50 mCi Rh matrix. The ideal thickness of the sample was evaluated considering the weight percentages of the different elements of each catalyst (approximately 100 mg of powder were used in a sample holder of about 1.8 cm in diameter). The reference used for velocity calibration was a 12 μm-thick α-Fe foil. The spectra were collected at 12 and 298 K. Measurements at low temperatures were performed using a closed-cycle cryogenic system (Model DE-202, ARS, Macungie, PA, USA). Each spectrum was folded to minimize geometric effects, and the experimental data were fitted using Recoil [41].

3.8. Catalytic Activity

For the catalytic evaluation, 200 mg of catalyst diluted in 1.5 g of ground and sieved quartz were used in each test, with the aim of obtaining homogeneity in the catalytic bed, which was placed in the center of a tubular quartz reactor of 12 mm in diameter. The reactor was placed inside an INDEF model T-150 furnace with a temperature controller. The reaction temperature was varied between 100 and 600 °C. A flow of 1000 ppm chlorobenzene diluted in synthetic air was bubbled from a thermostatic bath at −10 °C with a total feed rate of 200 mL/min. The reactants and products were analyzed online by gas chromatography using a Hewlett-Packard 5790A chromatograph equipped with a Carbowax 20 M/Chromosorb W column and a flame ionization detector (FID). (Figure 15) The total carbon balance was attained through the expression $\frac{CBin - CBout}{CBin}$. A bubbler was placed at the outlet of the reactor with 20 mL of a NaOH solution at 10% wt., which was used as a chlorine trap to prevent chlorine from passing to the chromatographic column, and to be able to carry out the determinations of the chlorinated products of the combustion reaction. This determination was found by bubbling a known volume of chlorinated effluent into a

solution of known KI concentration, followed by the titration of the released iodine with a solution of known $Na_2S_2O_3$ concentration, according to the procedure followed by Skoog DA et al. [42].
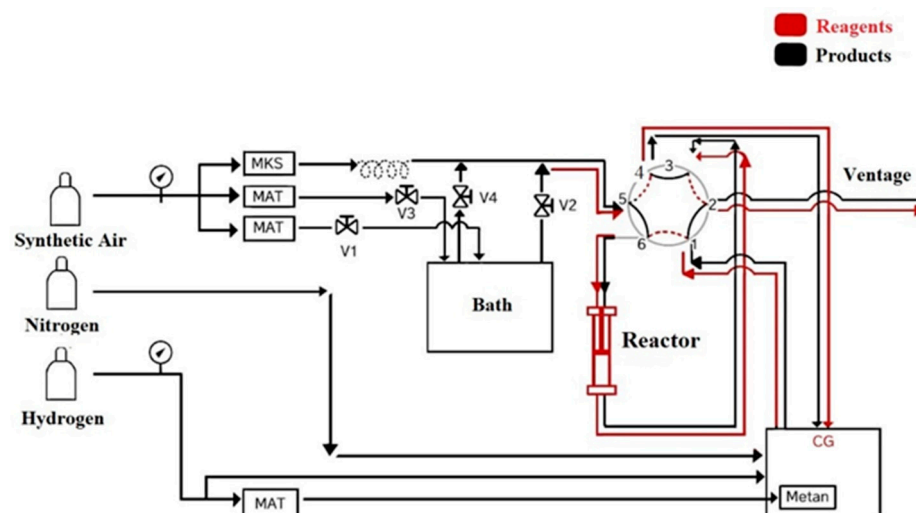

Figure 15. Schematic diagram of the catalytic activity test system.

4. Conclusions

In this work, a series of Fe-doped $LaCoO_3$ catalysts have been synthesized by the citrate method. In all cases, pure structures with orthorhombic and rhombohedral geometries were obtained according to the degree of substitution. For all the materials synthesized during the chlorobenzene combustion reaction, the total oxidation products were obtained at temperatures close to 500 °C. The most stable catalyst was the one with the lowest Fe substitution (x = 0.25), maintaining its invariable structure and activity after 100 h of time on stream. The insertion of Fe in small quantities favors the stability of the structure, not because of the existence of an unusually high oxidation state of Fe but due to the charge compensation produced by the existence of Co^{2+} that generates oxygen vacancies. All the results presented here confirm the potential properties of the $LaCo_{1-x}Fe_xO_3$ catalysts (x = 0.25) to remove chlorinated volatile organic compounds from industrial waste.

References

1. Guiotto, M.; Pacella, M.; Perin, G.; Iovino, A.; Michelon, N.; Natile, M.M.; Glisenti, A.; Canu, P. Washcoating vs. Direct Synthesis of $LaCoO_3$ on Monoliths for Environmental Applications. *Appl. Catal. A Gen.* **2015**, *499*, 146–157. [CrossRef]
2. De la Rosa, J.R.; Hernandez, A.; Rojas, F.; Ledezma, J.J. Sol-Gel Synthesis and Characterization of Novel La, Mn and Fe Doped Zirconia: Catalytic Combustion Activity of Trichloroethylene. *Colloids Surf. A Physicochem. Eng. Asp.* **2008**, *315*, 147–155. [CrossRef]
3. Lucio-Ortiz, C.J.; De La Rosa, J.R.; Ramirez, A.H.; De Los Reyes Heredia, J.A.; Del Angel, P.; Muñoz-Aguirre, S.; De León-Covián, L.M. Synthesis and Characterization of Fe Doped Mesoporous Al_2O_3 by Sol-Gel Method and Its Use in Trichloroethylene Combustion. *J. Sol-Gel Sci. Technol.* **2011**, *58*, 374–384. [CrossRef]
4. Michalik-Zym, A.; Dula, R.; Duraczyńska, D.; Kryściak-Czerwenka, J.; Machej, T.; Socha, R.P.; Włodarczyk, W.; Gaweł, A.; Matusik, J.; Bahranowski, K.; et al. Active, Selective and Robust Pd and/or Cr Catalysts Supported on Ti-, Zr- or [Ti,Zr]-Pillared Montmorillonites for Destruction of Chlorinated Volatile Organic Compounds. *Appl. Catal. B Environ.* **2015**, *174–175*, 293–307. [CrossRef]
5. Sinquin, G.; Hindermann, J.P.; Petit, C.; Kiennemann, A. Perovskites as Polyvalent Catalysts for Total Destruction of C1, C2 and Aromatic Chlorinated Volatile Organic Compounds. *Catal. Today* **1999**, *54*, 107–118. [CrossRef]
6. He, F.; Luo, J.; Liu, S. Novel Metal Loaded KIT-6 Catalysts and Their Applications in the Catalytic Combustion of Chlorobenzene. *Chem. Eng. J.* **2016**, *294*, 362–370. [CrossRef]
7. Acosta Perez, H.; Lopez, C.A.; Cadus, L.E.; Agüero, F.N. Evaluación Catalítica y estudio cinético diferencial de la reacción de combustión de Clorobenceno con catalizadores de LaCoO3 sustituidos con Ce. In *XXII Congreso Argentino de Catálisis*; CICAT: Santa Fe, Argentina, 2019; ISBN 9789874851703.
8. Schneider, U.; Hackermüller, L.; Will, S.; Best, T.; Bloch, I.; Costi, T.A.; Helmes, R.W.; Rasch, D.; Rosch, A. Metallic and Insulating Phases of Repulsively Interacting Fermions in a 3D Optical Lattice. *Science* **2008**, *322*, 1520–1525. [CrossRef]
9. Ojifinni, R.A.; Froemming, N.S.; Gong, J.; Pan, M.; Kim, T.S.; White, J.M.; Henkelman, G.; Mullins, C.B. Water-Enhanced Low-Temperature CO Oxidation and Isotope Effects on Atomic Oxygen-Covered Au(111). *J. Am. Chem. Soc.* **2008**, *130*, 6801–6812. [CrossRef]
10. Royer, S.; Duprez, D. Catalytic Oxidation of Carbon Monoxide over Transition Metal Oxides. *ChemCatChem* **2011**, *3*, 24–65. [CrossRef]
11. Hadri, A.E.L.; González-Calbet, J.M.; Alonso, A.G. Perovskitas Hexagonales de Hierro: Papel de La Subred Aniónica En La Oxidación Catalítica de CO. Inedit thesis, Universidad Complutense de Madrid, Facultad de Ciencias Químicas, Departamento de Química Inorgánica, Madrid, Spain, 2016.
12. Pérez, H.A.; López, C.A.; Cadús, L.E.; Agüero, F.N. Catalytic Feasibility of Ce-Doped $LaCoO_3$ Systems for Chlorobenzene Oxidation: An Analysis of Synthesis Method. *J. Rare Earths* **2021**, *40*, 897–905. [CrossRef]
13. Rietveld, H.M. A Profile Refinement Method for Nuclear and Magnetic Structures. *J. Appl. Crystallogr.* **1969**, *2*, 65–71. [CrossRef]
14. Rodríguez-Carvajal, J. Recent Advances in Magnetic Structure Determination by Neutron Powder Diffraction. *Phys. B Condens. Matter* **1993**, *192*, 55–69. [CrossRef]
15. Lagarec, K. *Recoil User Manual—Mossbauer Spectral Analysis Software for Windows*; University of Ottawa: Ottawa, ON, Canada, 1998.
16. Skoog, D.A.; West, D.M.; Holler, J.; Crouch, S.R. *Preparación de Disoluciones Estándar Básicas*; Reverté S.A. Spain: Barcelona, Spain, 2015; ISBN 9780495558286.
17. Kamal, M.S.; Razzak, S.A.; Hossain, M.M. Catalytic Oxidation of Volatile Organic Compounds (VOCs)—A Review. *Atmos. Environ.* **2016**, *140*, 117–134. [CrossRef]
18. Rochard, G.; Olivet, L.; Tannous, M.; Poupin, C.; Siffert, S.; Cousin, R. Recent Advances in the Catalytic Treatment of Volatile Organic Compounds: A Review Based on the Mixture Effect. *Catalysts* **2021**, *11*, 1218. [CrossRef]
19. Wang, Y.; Wang, G.; Deng, W.; Han, J.; Qin, L.; Zhao, B.; Guo, L.; Xing, F. Study on the Structure-Activity Relationship of Fe-Mn Oxide Catalysts for Chlorobenzene Catalytic Combustion. *Chem. Eng. J.* **2020**, *395*, 125172. [CrossRef]
20. Li, X.; Liu, Y.; Lin, C.; Wang, Y.; Lei, Z.; Xiong, P.; Luo, Y.; Chen, Q.; Zeng, L.; Wei, M.; et al. Structure Engineering of $BiSbS_x$ Nanocrystals Embedded within Sulfurized Polyacrylonitrile Fibers for High Performance of Potassium-Ion Batteries. *Chem.–A Eur. J.* **2022**, *28*, e202200028. [CrossRef]
21. Bedel, L.; Roger, A.C.; Estournes, C.; Kiennemann, A. Co^0 from Partial Reduction of $La(Co,Fe)O_3$ Perovskites for Fischer-Tropsch Synthesis. *Catal. Today* **2003**, *85*, 207–218. [CrossRef]
22. Merino, N.A.; Barbero, B.P.; Grange, P.; Cadús, L.E. $La_{1-x}Ca_xCoO_3$ Perovskite-Type Oxides: Preparation, Characterisation, Stability, and Catalytic Potentiality for the Total Oxidation of Propane. *J. Catal.* **2005**, *231*, 232–244. [CrossRef]
23. Merino, N.A.; Barbero, B.P.; Ruiz, P.; Cadús, L.E. Synthesis, Characterisation, Catalytic Activity and Structural Stability of $LaCo_{1-y}Fe_yO_{3\pm\lambda}$ Perovskite Catalysts for Combustion of Ethanol and Propane. *J. Catal.* **2006**, *240*, 245–257. [CrossRef]
24. Ciambelli, P.; Cimino, S.; Lisi, L.; Faticanti, M.; Minelli, G.; Pettiti, I.; Porta, P. La, Ca and Fe Oxide Perovskites: Preparation, Characterization and Catalytic Properties for Methane Combustion. *Appl. Catal. B Environ.* **2001**, *33*, 193–203. [CrossRef]
25. Aguero, F.N.; Scian, A.; Barbero, B.P.; Cadús, L.E. Combustion of Volatile Organic Compounds over Supported Manganese Oxide: Influence of the Support, the Precursor and the Manganese Loading. *Catal. Today* **2008**, *133–135*, 493–501. [CrossRef]

26. Goldwasser, M.R.; Rivas, M.E.; Lugo, M.L.; Pietri, E.; Pérez-Zurita, J.; Cubeiro, M.L.; Griboval-Constant, A.; Leclercq, G. Combined Methane Reforming in Presence of CO_2 and O_2 over $LaFe_{1-X}Co_xO_3$ Mixed-Oxide Perovskites as Catalysts Precursors. *Catal. Today* **2005**, *107–108*, 106–113. [CrossRef]

27. Koehler, W.C.; Wollan, E.O. Neutron-Diffraction Study of the Magnetic Properties of Perovskite-like Compounds $LaBO_3$. *J. Phys. Chem. Solids* **1957**, *2*, 100–106. [CrossRef]

28. Berry, F.J.; Ren, X.; Gancedo, J.R.; Marco, J.F. 57Fe Mössbauer Spectroscopy Study of $LaFe_{1-X}Co_xO_3$ (x = 0 and 0.5) Formed by Mechanical Milling. *Hyperfine Interact.* **2004**, *156–157*, 335–340. [CrossRef]

29. Berry, F.J.; Gancedo, J.R.; Marco, J.F.; Ren, X. Synthesis and Characterization of the Reduction Properties of Cobalt-Substituted Lanthanum Orthoferrites. *J. Solid State Chem.* **2004**, *177*, 2101–2114. [CrossRef]

30. Troyanchuk, I.O.; Karpinskiĭ, D.V.; Dobryanskiĭ, V.M.; Fedotova, Y.A.; Szymczak, H. The Two-Phase Crystal Structure and Magnetic Properties of the $LaCo_{1-X}Fe_xO_{3-d}$ System. *J. Exp. Theor. Phys.* **2005**, *100*, 1121–1126. [CrossRef]

31. Popov, N.; Bošković, M.; Perović, M.; Németh, Z.; Wang, J.; Kuang, Z.; Reissner, M.; Kuzmann, E.; Homonnay, Z.; Kubuki, S.; et al. Influence of Low-Spin Co^{3+} for High-Spin Fe^{3+} Substitution on the Structural, Magnetic, Optical and Catalytic Properties of Hematite (α-Fe_2O_3) Nanorods. *J. Phys. Chem. Solids* **2021**, *152*, 109929. [CrossRef]

32. Russo, U.; Nodari, L.; Faticanti, M.; Kuncser, V.; Filoti, G. Local Interactions and Electronic Phenomena in Substituted $LaFeO_3$ Perovskites. *Solid State Ionics* **2005**, *176*, 97–102. [CrossRef]

33. Barbero, B.P.; Cadús, L.E.; Marchetti, S.G. Determination of Fe(IV) Species in Partially Substituted Perovskite $La_{0.6}Ca_{0.4}FeO_3$. *Hyperfine Interact.* **2009**, *194*, 367–379. [CrossRef]

34. Wang, X.; Jin, B.; Feng, R.; Liu, W.; Weng, D.; Wu, X.; Liu, S. A Robust Core-Shell Silver Soot Oxidation Catalyst Driven by Co_3O_4: Effect of Tandem Oxygen Delivery and Co_3O_4-CeO_2 Synergy. *Appl. Catal. B Environ.* **2019**, *250*, 132–142. [CrossRef]

35. Lv, C.; Zhang, J.; Yan, L.; Chen, H.; Hu, M. Boosting Sulfur Tolerance and Catalytic Performance in Toluene Combustion Via Enhanced-Mechanism of Ce-Fe Dopants Incorporation Of $LaCoO_3$ Perovskite. *SSRN Electron. J.* **2022**, *10*, 108372. [CrossRef]

36. Biesinger, M.C.; Payne, B.P.; Grosvenor, A.P.; Lau, L.W.M.; Gerson, A.R.; Smart, R.S.C. Resolving Surface Chemical States in XPS Analysis of First Row Transition Metals, Oxides and Hydroxides: Cr, Mn, Fe, Co and Ni. *Appl. Surf. Sci.* **2011**, *257*, 2717–2730. [CrossRef]

37. Song, S.; Zhang, C.; Lou, Y.; Wu, Y.; Wang, L.; Guo, Y.; Zhan, W.; Guo, Y. Effects of Water on CO Catalytic Oxidation over Pd/CeO_2. *J. Rare Earths* **2020**, *38*, 891–898. [CrossRef]

38. Lago, R.; Bini, G.; Peña, M.A.; Fierro, J.L.G. Partial Oxidation of Methane to Synthesis Gas Using $LnCoO_3$ Perovskites as Catalyst Precursors. *Stud. Surf. Sci. Catal.* **1997**, *110*, 721–730. [CrossRef]

39. McCarty, J.G.; Wise, H. Perovskite Catalysts for Methane Combustion. *Catal. Today* **1990**, *8*, 231–248. [CrossRef]

40. Shannon, R.D. Revised Effective Ionic Radii and Systematic Studies of Interatomic Distances in Halides and Chalcogenides. *Acta Crystallogr. Sect. A* **1976**, *32*, 751–767. [CrossRef]

41. Bello, I.; Chang, W.H.; Lau, W.M. Mechanism of Cleaning and Etching Si Surfaces with Low Energy Chlorine Ion Bombardment. *J. Appl. Phys.* **1994**, *75*, 3092–3097. [CrossRef]

42. Zhu, J.; Zhang, W.; Qi, Q.; Zhang, H.; Zhang, Y.; Sun, D.; Liang, P. Catalytic Oxidation of Toluene, Ethyl Acetate and Chlorobenzene over Ag/MnO_2-Cordierite Molded Catalyst. *Sci. Rep.* **2019**, *9*, 12162. [CrossRef]